nature nanotechnology

Article

https://doi.org/10.1038/s41565-023-01397-0

Engineering metal oxidation using epitaxial strain

Received: 2 August 2022

Accepted: 13 April 2023

Published online: 22 May 2023

Check for updates

Sreejith Nair[1] ✉, Zhifei Yang[1,2], Dooyong Lee[1], Silu Guo[1], Jerzy T. Sadowski[3], Spencer Johnson[4], Abdul Saboor[5], Yan Li[6], Hua Zhou[7], Ryan B. Comes[4], Wencan Jin[4], K. Andre Mkhoyan[1], Anderson Janotti[5] & Bharat Jalan[1] ✉

The oxides of platinum group metals are promising for future electronics and spintronics due to the delicate interplay of spin-orbit coupling and electron correlation energies. However, their synthesis as thin films remains challenging due to their low vapour pressures and low oxidation potentials. Here we show how epitaxial strain can be used as a control knob to enhance metal oxidation. Using Ir as an example, we demonstrate the use of epitaxial strain in engineering its oxidation chemistry, enabling phase-pure Ir or IrO_2 films despite using identical growth conditions. The observations are explained using a density-functional-theory-based modified formation enthalpy framework, which highlights the important role of metal-substrate epitaxial strain in governing the oxide formation enthalpy. We also validate the generality of this principle by demonstrating epitaxial strain effect on Ru oxidation. The IrO_2 films studied in our work further revealed quantum oscillations, attesting to the excellent film quality. The epitaxial strain approach we present could enable growth of oxide films of hard-to-oxidize elements using strain engineering.

Most metals found in nature are known to spontaneously form an oxide layer on the surface. Yet there are some metals like gold, silver and the platinum group metals that have low oxidation potentials and hence require high temperature and oxygen pressure to form oxides[1,2]. The 'stubborn'[3] nature of these metals makes it challenging to grow their oxide thin films using ultra-high vacuum (UHV) physical vapour deposition techniques. Substantial efforts have been made to achieve high-quality epitaxial growth[4–7] owing to the unconventional properties that these materials possess[8–12]. Even the simple binary oxides of metals like Ru and Ir host novel electronic, magnetic and topological properties[13–17]. Whether we can harness the potential of these stubborn metal oxides depends on our ability to address the oxidation challenge and to synthesize built-to-order material structures with controlled composition, structure and dimensionality.

The growth conditions required for metal oxidation are commonly informed using an Ellingham diagram that is based on thermodynamic free-energy considerations[18]. However, for the stubborn metals such as Ir, the oxygen pressure required for thermodynamically favoured oxide growth is higher than the permissible limit in a UHV technique. The most followed route to overcome this UHV constraint is the use of reactive oxygen species like ozone or oxygen plasma[19–21]. Epitaxial oxide growth conditions can also be driven by kinetic factors that affect film growth rate. It has been shown that the adsorption-controlled growth window for phase-pure $PbTiO_3$ depends strongly on the reactant fluxes and oxidation kinetics[22]. A similar report also exists for pulsed laser deposited $La_{0.7}Sr_{0.3}MnO_3$ where the laser fluence and plume characteristics were modified to achieve phase-pure oxide growth under significantly reduced oxygen pressures[23].

[1]Department of Chemical Engineering and Materials Science, University of Minnesota, Minneapolis, MN, USA. [2]School of Physics and Astronomy, University of Minnesota, Minneapolis, MN, USA. [3]Center for Functional Nanomaterials, Brookhaven National Laboratory, Upton, NY, USA. [4]Department of Physics, Auburn University, Auburn, AL, USA. [5]Department of Materials Science and Engineering, University of Delaware, Newark, DE, USA. [6]Materials Science Division, Argonne National Laboratory, Lemont, IL, USA. [7]X-ray Science Division, Advanced Photon Source, Argonne National Laboratory, Lemont, IL, USA. ✉e-mail: nair0074@umn.edu; bjalan@umn.edu

https://doi.org/10.1038/s41565-023-01397-0

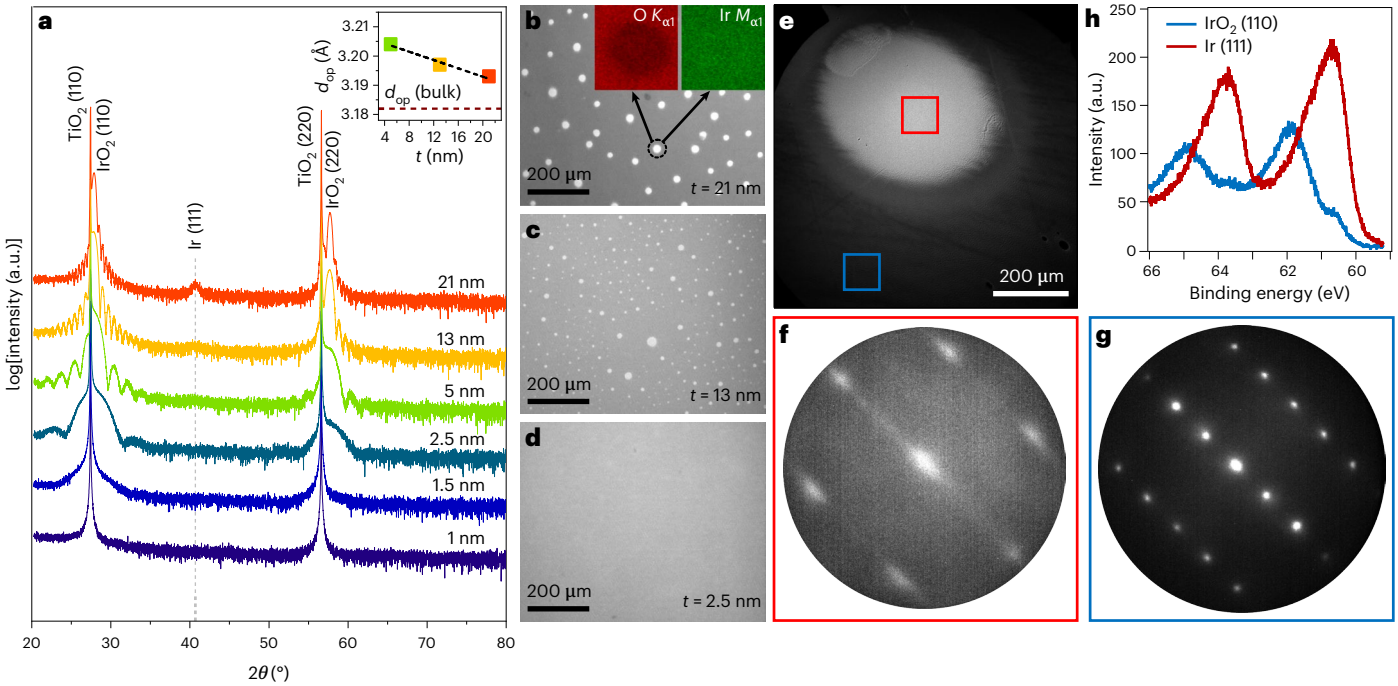

Fig. 1 | Surface Ir metal formation with increasing film thickness. a, XRD 2θ–ω coupled scans for IrO_2 (110) films of different thicknesses grown on TiO_2 (110) substrates (Laue oscillations can be observed around the IrO_2 (110) and (220) Bragg peaks for film thickness greater than 1.5 nm indicating excellent crystallinity) (inset: out of plane lattice parameter (d_{op}) of the IrO_2 films plotted against film thickness t). **b**–**d**, Surface optical microscope images for films with thickness 21 nm (**b**; inset: EDX map for oxygen K-edge and Ir M-edge showing an oxygen deficiency in the spot-like feature), 13 nm (**c**) and 2.5 nm (**d**). **e**, LEEM image of a spot-like surface feature on a 23 nm IrO_2 (110) film (grown at the same condition as the samples shown in **a** and Fig. 2) acquired at 1.1 eV electron energy. Red and blue boxes enclose the area where XPS and micro-LEED data are acquired. **f**,**g**, Micro-LEED patterns of Ir (111) (**f**) and IrO_2 (110) (**g**) acquired using 50 eV electron energy. **h**, XPS spectra acquired using 250 eV photon energy showing the presence of Ir^0 and Ir^{4+} on and off the spot-like feature (as shown in **e**), respectively.

However, a subtle aspect in epitaxial growth that has been challenging to incorporate in the thermokinetic framework for metal oxide formation is the effect of epitaxial strain. Even though there have been numerous studies investigating the effect of epitaxial strain on defect formation[24,25], crystal structure[26,27] and the resulting electronic and magnetic properties in oxides[28,29], the influence of strain on the free energy and kinetics of the metal to oxide chemistry and crystal formation remains unexplored. More importantly, as the film grows thicker, strain energy increases, which can lead to a higher energy penalty for continued growth of an epitaxially strained oxide crystal. So an intriguing question that arises is whether a difference in substrate-imposed epitaxial strain can affect the tendency of a metal atom to react with oxygen to promote an epitaxial oxide crystal and whether this tendency changes as volumetric strain energy increases with film thickness.

In this Article, using the solid-source metal-organic molecular beam epitaxy (MBE) technique[3], we provide experimental evidence for the effect of epitaxial strain on IrO_2 formation energy by studying the evolution of structure and composition, as we tune the epitaxial strain state and film thickness. We also developed a theoretical framework using first-principles-based density functional theory (DFT) calculations to explain this strain effect on metal oxidation. The strain effect on metal oxidation was also experimentally shown for Ru metal which attests to the generality of the proposed effect. Our work provides a new lens to study atomically precise epitaxial oxide thin-film growth and thereby facilitate the discovery of intriguing quantum properties in these materials.

An alternative approach to IrO_2 thin-film growth

We use a modified MBE synthesis approach by using a solid Ir containing metal organic precursor instead of pure elemental metal as our Ir source. This provides multiple advantages for UHV thin-film growth as described in detail in Methods.

Using an optimized substrate temperature of 300 °C, IrO_2 (110) films were grown on single-crystalline TiO_2 (110) substrates. Epitaxial thin films with increasing thicknesses were obtained by adjusting the duration of the co-deposition process. Figure 1a shows the on-axis 2θ–ω coupled X-ray diffraction (XRD) patterns of as-grown IrO_2 films. For film thickness up to 2.5 nm, the XRD scans show phase-pure, single-crystalline IrO_2 growth. However, a further increase in thickness results in the appearance of an ambiguous Ir (111) peak which evolves into a well-defined Ir (111) peak for a thickness of 21 nm. So above a critical thickness, Ir metal formation occurs, and the amount of Ir increases with thickness despite maintaining the same growth conditions.

Strain-relaxation-induced Ir metal formation

IrO_2 (110) on TiO_2 (110) is a highly anisotropically strained film and hence has a strong tendency to strain-relax[30]. The inset of Fig. 1a shows that the out of plane lattice parameter is decreasing with increasing film thickness, indicating that strain relaxation has occurred for film thickness as low as 5 nm. This can also be inferred from the synchrotron X-ray crystal truncation rod (CTR) scattering intensity for IrO_2 (110) films shown in Supplementary Fig. 1. The CTR scans for a 5-nm-thick film show persistent Laue oscillations in the specular 00L and off-specular 20L reflections, indicative of a high film quality and coherent epitaxial growth along the [1$\bar{1}$0] direction. On the contrary, due to the large epitaxial strain (−6.03%) along the [001] direction, the 01L CTR intensity shows no Laue oscillations indicative of enhanced strain relaxation in this direction, likely through formation of dislocations. The presence of dislocations was confirmed using high-resolution high-angle annular dark-field scanning transmission electron

https://doi.org/10.1038/s41565-023-01397-0

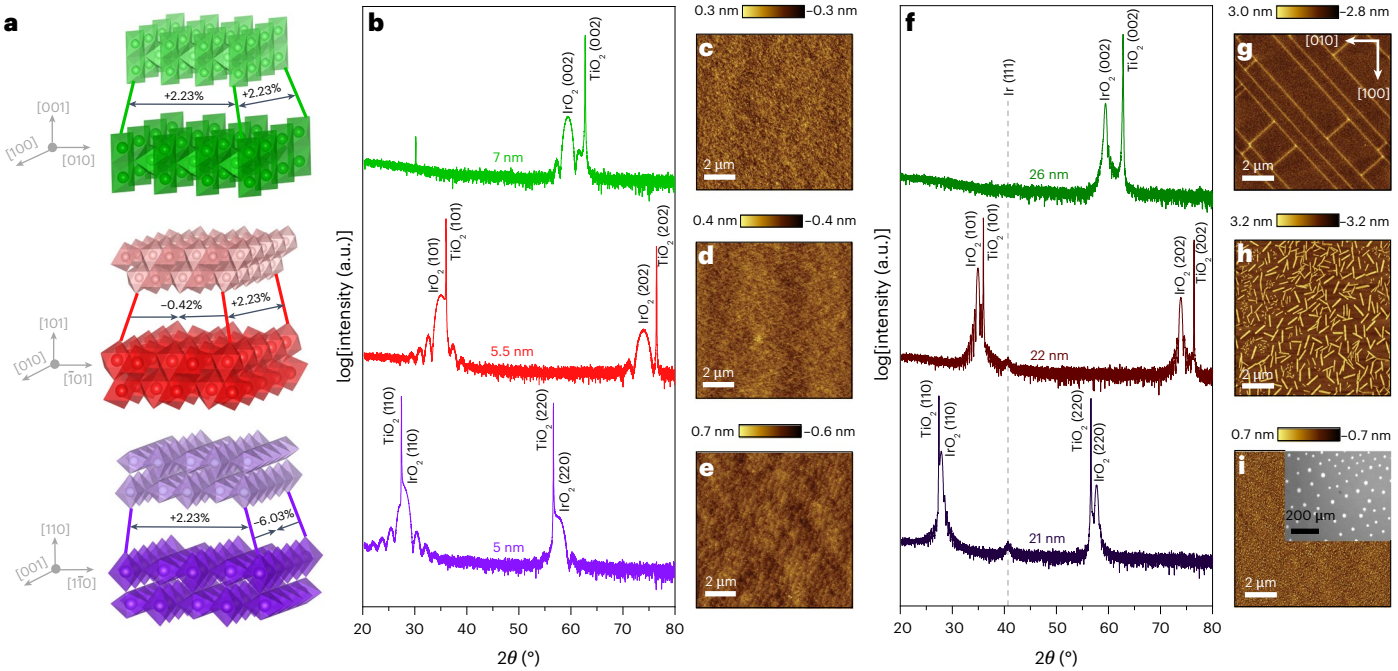

Fig. 2 | Varying thickness-dependent structural evolution as a function of epitaxial strain. a, Schematic showing the epitaxial strain states for IrO_2 films grown on (top to bottom) (001), (101) and (110) oriented TiO_2 substrates. **b**, XRD 2θ–ω coupled scans for thin IrO_2 films grown on different orientations of TiO_2 substrates. **c**–**e**, Corresponding AFM images showing atomically smooth surfaces with root mean square roughness less than 3 Å for the (001) (**c**), (101) (**d**) and (110) (**e**) oriented IrO_2 films. **f**, XRD 2θ–ω coupled scans for thicker IrO_2 films grown on different orientations of TiO_2 substrates. **g**–**i**, Corresponding AFM images showing well-defined cracks along family of planes for IrO_2 (001) (**g**), rod-shaped Ir metal features on the surface of IrO_2 (101) (**h**) and a smooth surface for IrO_2 (110) (**i**) with inset: spot-like surface Ir metal features observed in optical microscopy. The large epitaxial strain (~32% along both directions) for Ir (111) on IrO_2 (110) surface (as shown in Supplementary Fig. 12-1) could have led to a disk-like shape, whereas a lower lattice mismatch (-0.67% along one direction) for Ir (111) on IrO_2 (101) surface (as shown in Supplementary Fig. 10-1) may have caused the islands to adopt a rod-like morphology.

microscopy (HAADF-STEM) for a 21 nm IrO_2 (110) film as shown in Supplementary Fig. 2. Corresponding geometric phase analysis (GPA) and lattice column reconstruction using inverse fast Fourier transform shown in Supplementary Fig. 3 further reveal local hotspots in the strain fields and aid visualization of the dislocations. The thickness-dependent dislocation-driven strain relaxation and concurrent Ir metal formation hence lead to two possible hypotheses. (1) As the amount of Ir metal is observed to increase with thickness, Ir metal could be present in the bulk of all films and is simply a result of incomplete Ir oxidation. (2) Ir metal formation could be a strain-relaxation mechanism in addition to misfit dislocation formation because of the large anisotropic epitaxial strain.

The first hypothesis is addressed in Fig. 1b–d where distinct surface features were observed in the optical microscope images as film thickness was increased, which also correlates with increasing Ir(111) peak intensity in XRD. The chemical nature of these surface features was investigated using scanning electron microscopy (SEM) combined with energy-dispersive X-ray spectroscopy (EDX) (Fig. 1b, inset). EDX shows an oxygen deficiency within the spot-like feature. The film surface was also characterized using low-energy electron microscopy and diffraction (LEEM and LEED) (Fig. 1e–g). The micro-LEED patterns on and off the feature further provide definitive evidence for the predominant Ir(111) crystallinity of the Ir particles on the surface of the IrO_2 (110) film. The corresponding spatially resolved X-ray photoelectron spectra (XPS) (Fig. 1h) also confirm the presence of Ir metal in the spot-like features. Some of the spots, however, also contained amorphous or disordered Ir metal as observed from the unresolved black regions in the electron back-scatter diffraction (EBSD) map shown in Supplementary Fig. 4. The presence of amorphous Ir could be attributed to growth stress and the large epitaxial strain on Ir(111) crystal growing on the TiO_2 (110) surface. Cross-section HAADF-STEM images shown in Supplementary Fig. 2 further confirm the absence of any Ir islands in the bulk of the film. The surface-confined nature of these features, the fact that they were not observed at low thicknesses and the IrO_2 film quality (evidenced by Laue oscillations in XRD and CTR scans shown in Fig. 1a and Supplementary Fig. 1, respectively, along with quantum oscillations in magnetoresistance as shown in Supplementary Fig. 5) even in the presence of Ir features suggest that Ir metal formation need not be a trivial case of insufficient oxygen supply but instead could be driven by epitaxial strain relaxation.

The second hypothesis of strain-relaxation-induced Ir metal formation was hence investigated by growing IrO_2 films with different epitaxial strain states. The ideal way would have been to grow IrO_2 (110) film on a substrate that offers a considerably different strain state when compared with a TiO_2 (110) substrate. However, there are no commercially available rutile substrates that meet this criterion. MgO, which is a cubic substrate, has been reported to support epitaxial growth of RuO_2 and IrO_2 (110)[31]. However, the large in-plane strain and 45° rotated epitaxial relationship with the substrate may lead to the formation of twin domains and other defects, and hence, MgO does not serve as an ideal choice. Instead, IrO_2 films were grown on different orientations of TiO_2 substrates using the same conditions as described before. The different out-of-plane orientations allow us to achieve different epitaxial strain states, albeit at the cost of introducing a different IrO_2 surface in each case, as shown in Fig. 2a. It was observed that at low thickness, phase-pure IrO_2 films were obtained, irrespective of the growth orientation and epitaxial strain state, as shown in the XRD patterns in Fig. 2b. All films showed smooth surfaces in atomic force microscopy (AFM) as shown in Fig. 2c–e. However, at thicknesses larger than 20 nm, distinct film compositions and surface features were observed for each film orientation. Similar to IrO_2 (110), the IrO_2 (101) film also showed a thickness-dependent emergence of Ir (111) peak

https://doi.org/10.1038/s41565-023-01397-0

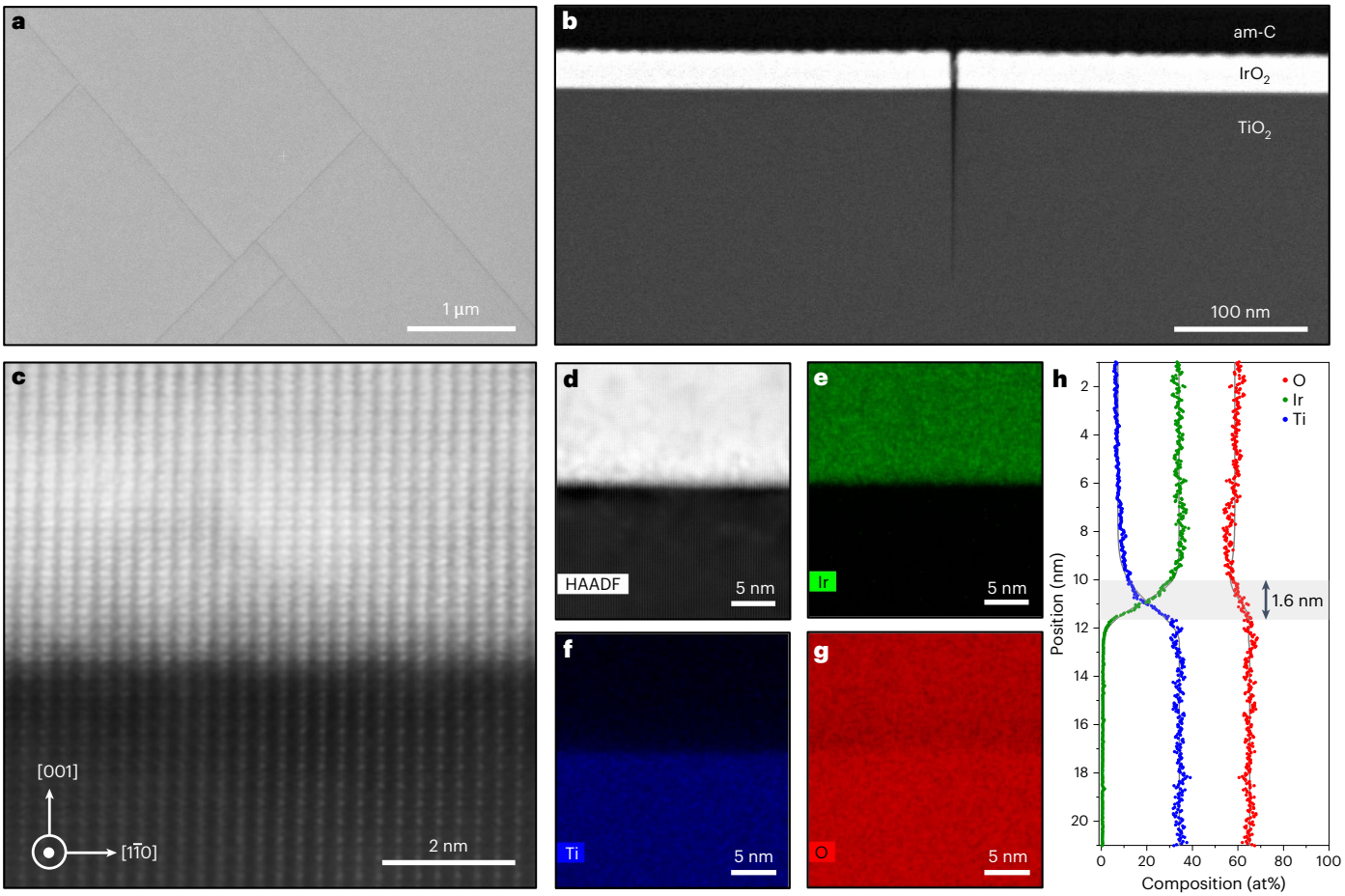

Fig. 3 | Microstructure of 26 nm IrO_2 (001) using SEM, STEM and elemental EDX mapping. a, SEM image of IrO_2 surface showing crack positions as dark lines. **b**, Low-magnification HAADF-STEM image of the cross-sectional sample: IrO_2 layer (26 nm) on top of TiO_2 substrate. **c**, Atomic-resolution HAADF-STEM image of the interface between IrO_2 and TiO_2. **d**–**h**, HAADF-STEM image (**d**) and complementary elemental EDX maps for Ir (**e**), Ti (**f**) and O (**g**) with line scan analysis (**h**) showing compositional variation at the interface (~1.6 nm). Grey lines are fitted curves.

in XRD as shown in Fig. 2f, accompanied by the formation of rod-like surface features as observed in the corresponding AFM image shown in Fig. 2h. Corresponding cross-section HAADF-STEM images confirm that the Ir metal features are confined to the surface as shown in Supplementary Fig. 6. A point of dissimilarity between the two different film orientations, however, shows up in the film rocking curves plotted in Supplementary Fig. 7. Unlike IrO_2 (110), the IrO_2 (101) film, due to a lower magnitude of anisotropic strain, maintains a nearly constant full width at half maximum with thickness, suggesting that there is almost no strain-relaxation-induced structural disorder in the bulk of the film. This is further supported by the highly coherent IrO_2 film structure as observed in the HAADF-STEM image shown in Supplementary Fig. 6.

Competing strain-relaxation mechanisms

Contrary to the (110) and (101) orientations, the IrO_2 (001) film, as observed from XRD shown in Fig. 2f, surprisingly did not show Ir formation with increasing thickness. Instead, the film was observed to strain relax by forming well-defined cracks as shown in the AFM image in Fig. 2g. The presence of cracks was confirmed using SEM imaging (Fig. 3a), and cracks were found to penetrate into the substrate as observed from the low-magnification HAADF-STEM image in Fig. 3b. Crack penetration into the substrate has been reported previously for RuO_2 on TiO_2 (110) substrate and is attributed to the strong interfacial bonding between the film and the substrate[17]. A case for crack propagation into the substrate can also be made based on the surface energy of the cleaved[32] planes as shown in Supplementary Fig. 8. Although extensive cracking occurred, the rocking curve full width at half maximum as shown in Supplementary Fig. 7 remained constant with thickness, similar to the IrO_2 (101) films. This is further corroborated by the atomic-resolution HAADF-STEM image of the region between the cracks in Fig. 3c, which shows a dislocation-free, highly coherent film with near atomically sharp film-substrate interface, despite the large tensile strain state. The elemental composition probed using STEM-EDX mapping as shown in Fig. 3d–h also shows distinct chemical interfaces and a uniform oxygen concentration profile.

The thickness-dependent structural evolution of the different film orientations thus reveal competing strain-relaxation mechanisms. The observations on IrO_2 (110) and IrO_2 (101) point to Ir metal formation as a possible strain-relaxation or strain energy minimization mechanism. At the same time, the absence of such a mechanism in IrO_2 (001) despite the same growth conditions helps refute the idea that Ir metal formation is simply due to insufficient supply of oxygen. It also highlights the role of epitaxial strain on IrO_2 crystal formation energy and how strain-induced changes in formation energies can govern the strain-relaxation mechanism. However, if Ir formation is indeed a strain-relaxation behaviour, then eliminating Ir formation by increasing the oxygen chemical potential should force the film to relax through a different mechanism. This dependence of oxygen chemical potential was verified by growing IrO_2 (110) film of comparable thickness at an oxygen pressure ~1.6 times higher than that used for all other films described above. Figure 4a shows that the IrO_2 (110) film, when grown at higher oxygen pressure, shows no evidence of Ir metal formation

https://doi.org/10.1038/s41565-023-01397-0

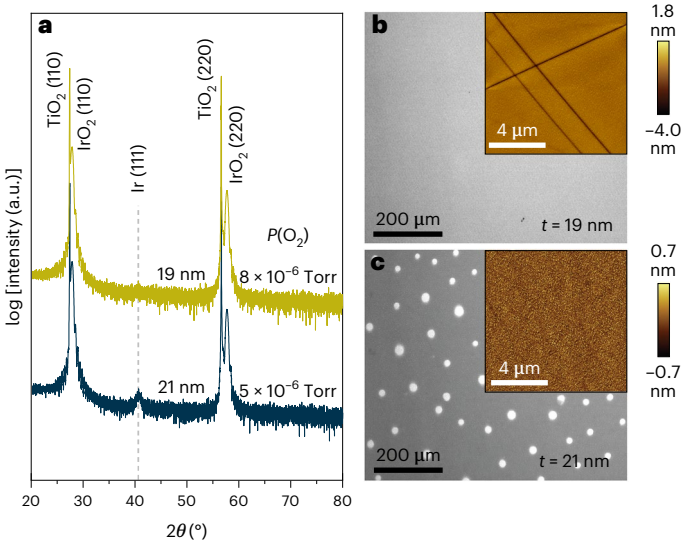

Fig. 4 | Effect of oxygen pressure on strain-relaxation mechanism. a, XRD 2θ–ω coupled scans for IrO_2 (110) films grown on TiO_2 (110) substrates under different oxygen pressure conditions. **b**,**c**, Corresponding surface optical microscope images for the two IrO_2 (110) films with $t = 19$ nm (**b**) and $t = 21$ nm (**c**). Inset: AFM images showing the emergence of cracks when films are grown at higher oxygen pressure.

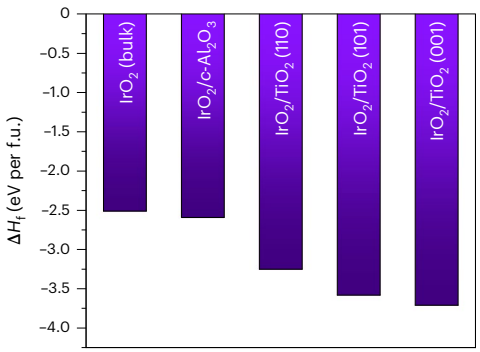

Fig. 5 | DFT calculations of formation enthalpy as a function of epitaxial strain. Calculated formation enthalpy using DFT with the generalized gradient approximation for bulk single-crystal IrO_2 and IrO_2 when grown as an epitaxially strained film on various substrates for a fixed oxygen chemical potential. A modified definition as described in the main text (where formation enthalpy is defined with respect to epitaxially strained Ir as the reactant with oxygen) was used to calculate the formation enthalpies.

in XRD. The absence of Ir (111) peak in XRD is accompanied by loss of surface Ir features as observed from the optical microscope images shown in Fig. 4b,c. More importantly, at higher oxygen pressures where Ir formation is thermodynamically unfavourable, the film strain relaxed by forming well-defined cracks as observed from the AFM image shown in the inset of Fig. 4b. This observation again suggests that Ir formation is a competing strain-relaxation mechanism, and oxygen pressure can affect the relaxation mechanism.

Quantifying the strain effect on oxide formation energy

While our experimental evidence suggests that Ir formation or the difficulty to form an epitaxial IrO_2 crystal above a certain thickness is related to epitaxial strain, it does not reveal why an anisotropic strain state in the (110) and (101) oriented films leads to Ir formation as opposed to an isotropic strain in the (001) oriented film. To answer this, a rigorous analysis would require simulating the epitaxial growth process while integrating the reaction energetics and multiple competing strain-relaxation mechanisms for the different strain states. However, this turns out to be a challenging and computationally expensive task due to the dynamic and non-equilibrium nature of epitaxial growth process. Hence, we instead turn to a simple and more tractable approach by revisiting the definition of formation enthalpy of a crystal. The standard state formation enthalpy of any material is defined as the enthalpy of the products minus the enthalpy of the reactants at standard state conditions. So in the bulk regime, formation enthalpy for IrO_2 would be defined as shown in equation (1), where $E_{tot}(IrO_2)$, $E_{tot}(Ir)$ and $E_{tot}(O_2)$ represent the enthalpy at standard state conditions for bulk IrO_2 crystal, bulk Ir crystal and O_2 molecule, respectively.

$$\Delta H_f = E_{tot}(IrO_2) - E_{tot}(Ir) - E_{tot}(O_2) \quad (1)$$

However, for epitaxial thin films where the crystals are strained, the standard state enthalpy of the product would change and so would the formation or reaction enthalpy. Conventionally this approach only takes into account the strain in the as-grown film that is the product and does not take into account any strain effect on the reactants, which intuitively makes sense. However, because we observe in our experiments a possible effect of strain on the oxidation behaviour of the metal, which is the reactant, we define the formation energy of a strained bulk IrO_2 crystal with respect to strained bulk Ir metal crystal (referred to as 'epi' in equation (2)), as opposed to relaxed bulk Ir metal crystal. Strain is applied to bulk phases for the calculations to avoid complications arising from the choice of termination and interfacial effects. As shown in equation (1), the formation enthalpy, which is used as a proxy for the Gibbs' free energy of formation, now also depends on how the reactant metal interacts with the growth front.

$$\Delta H_f = E_{tot}(IrO_2 - epi) - E_{tot}(Ir - epi) - E_{tot}(O_2) \quad (2)$$

This modified definition entails that making the Ir metal unstable by using a substrate that has a larger lattice mismatch with Ir metal (Supplementary Figs. 9–12) would favour the formation of IrO_2 by making the formation enthalpy more negative. The idea is similar in some way to the use of ozone or oxygen plasma, for example, where the oxygen species is made more reactive to drive the oxidation reaction. Using this approach, we calculated the formation energies for epitaxially strained IrO_2 on different substrates as shown in Fig. 5. We find that the (001) oriented IrO_2 on TiO_2 (001) substrate has the largest free energy of formation and, hence, is less prone to strain-relaxation-induced Ir formation. To further validate this model, we attempted to grow an IrO_2 film using the same growth conditions on a *c*-plane sapphire substrate, which is better lattice matched to the Ir (111) facet. We found that, for the same oxidation conditions where IrO_2 was obtained on TiO_2 substrates, we obtained phase-pure Ir (111) metal film as shown in Supplementary Fig. 13a. The growth of Ir metal was also confirmed using Ir 4f XPS as shown in Supplementary Fig. 13b, which only shows the presence of Ir^0 oxidation state. Corresponding IrO_2 formation energy on *c*-Al_2O_3 was also calculated to be lower than the different TiO_2 substrates, and hence, the applicability of such a model in epitaxial systems holds ground. Further, to test the generality of the modified formation enthalpy framework, we demonstrated this effect of strain on the oxidation of Ru. As shown in Supplementary Fig. 14, film grown using $Ru(acac)_3$ as the metal source and oxygen plasma on TiO_2 (110) substrate was observed to form RuO_2, whereas the same growth conditions resulted in epitaxial Ru metal when grown on *c*-Al_2O_3 substrate. The formation of a sixfold symmetric hexagonal close-packed Ru metal under strong oxidation condition was further verified using phi scans around the asymmetric $(\bar{2}114)$ peak for a representative sample as shown in the inset of Supplementary Fig. 14.

However, a more counterintuitive result from the calculated formation energies lies in the enhanced formation energy of strained IrO_2 crystal compared with a relaxed equilibrium IrO_2 crystal, which originates from the use of the modified formation energy definition. To show that this anomalous behaviour is indeed true for epitaxial oxide growth, we performed ex situ oxygen annealing of the IrO_2 (110) films with surface Ir metal features. We found that even after annealing the films under oxygen pressures ~10^8 times higher than the oxygen background pressures used during growth, there was only a gradual change in the Ir metal peak intensity as a function of annealing time and temperature, as observed from post-annealing XRD scans (Supplementary Fig. 15). This observation highlights a particularly important fact that the relaxed Ir metal present on the surface is difficult to oxidize, whereas the Ir metal supplied during vapour deposition to the substrate could be oxidized to IrO_2 even under high vacuum growth conditions. This reinforces the idea that the epitaxial interaction between the metal and the substrate plays a very important role in 'activating the metal', which is reflected in the enhanced calculated formation energy for epitaxially strained IrO_2 compared with bulk relaxed IrO_2.

Conclusions

Our work thus reveals, a new route to enhance metal oxidation and control the formation of different competing phases by strain engineering. A multi-faceted approach using thin-film growth, X-ray and electron diffraction, optical and electron microscopy, XPS, EDX and DFT calculations systematically confirmed the strain dependence of Ir to IrO_2 chemistry. This effect of strain, in combination with our synthesis approach, further allowed us to synthesize thin-film IrO_2 that shows quantum oscillations in magnetoresistance. The idea presented here can hence potentially have a major impact on the synthesis of various materials such as the higher 'n' members of the Ruddlesden–Popper phases and pyrochlore iridates which hold great potential for realizing exotic quantum phases[33–36] but have been experimentally challenging to synthesize due to their narrow or inaccessible thermodynamic growth windows[37,38].

Online content

Any methods, additional references, Nature Portfolio reporting summaries, source data, extended data, supplementary information, acknowledgements, peer review information; details of author contributions and competing interests; and statements of data and code availability are available at https://doi.org/10.1038/s41565-023-01397-0.

References

1. Novotny, Z. et al. Kinetics of the thermal oxidation of Ir(100) toward IrO_2 studied by ambient-pressure X-ray photoelectron spectroscopy. *J. Phys. Chem. Lett.* **11**, 3601–3607 (2020).
2. van Spronsen, M. A., Frenken, J. W. M. & Groot, I. M. N. Observing the oxidation of platinum. *Nat. Commun.* **8**, 429 (2017).
3. Nunn, W. et al. Novel synthesis approach for "stubborn" metals and metal oxides. *Proc. Natl Acad. Sci. USA* **118**, e2105713118 (2021).
4. Liu, X. R. et al. Synthesis and electronic properties of Ruddlesden–Popper strontium iridate epitaxial thin films stabilized by control of growth kinetics. *Phys. Rev. Mater.* **1**, 075004 (2017).
5. Nair, H. P. et al. Demystifying the growth of superconducting Sr_2RuO_4 thin films. *APL Mater.* **6**, 101108 (2018).
6. Nunn, W. et al. Solid-source metal-organic molecular beam epitaxy of epitaxial RuO_2. *APL Mater.* **9**, 091112 (2021).
7. Wakabayashi, Y. K. et al. Machine-learning-assisted thin-film growth: Bayesian optimization in molecular beam epitaxy of $SrRuO_3$ thin films.*APL Mater.* **7**, 101114 (2019).
8. Kim, B. J. et al. Phase-sensitive observation of a spin-orbital Mott state in Sr_2IrO_4. *Science* **323**, 1329–1332 (2009).
9. Kim, W. J. et al. Strain engineering of the magnetic multipole moments and anomalous Hall effect in pyrochlore iridate thin films.*Sci. Adv.* **6**, eabb1539 (2020).
10. Kim, Y. K., Sung, N. H., Denlinger, J. D. & Kim, B. J. Observation of a *d*-wave gap in electron-doped Sr_2IrO_4. *Nat. Phys.* **12**, 37–41 (2016).
11. Kushwaha, P. et al. Nearly free electrons in a 5*d* delafossite oxide metal. *Sci. Adv.* **1**, e1500692 (2015).
12. Nelson, J. N. et al. Interfacial charge transfer and persistent metallicity of ultrathin $SrIrO_3/SrRuO_3$ heterostructures. *Sci. Adv.* **8**, eabj0481 (2022).
13. Zhu, Z. H. et al. Anomalous antiferromagnetism in metallic RuO_2 determined by resonant X-ray scattering. *Phys. Rev. Lett.* **122**, 017202 (2019).
14. Uchida, M. et al. Field-direction control of the type of charge carriers in nonsymmorphic IrO_2. *Phys. Rev. B* **91**, 241119 (2015).
15. Smejkal, L., Gonzalez-Hernandez, R., Jungwirth, T. & Sinova, J. Crystal time-reversal symmetry breaking and spontaneous Hall effect in collinear antiferromagnets. *Sci. Adv.* **6**, eaaz8809 (2020).
16. Nelson, J. N. et al. Dirac nodal lines protected against spin-orbit interaction in IrO_2. *Phys. Rev. Mater.* **3**, 064205 (2019).
17. Ruf, J. P. et al. Strain-stabilized superconductivity. *Nat. Commun.* **12**, 59 (2021).
18. Ellingham, H. J. T. Reducibility of oxides and sulphides in metallurgical processes. *J. Soc. Chem. Ind. Trans. Commun.* **63**, 125–160 (1944).
19. Chambers, S. A. Epitaxial growth and properties of thin film oxides. *Surf. Sci. Rep.* **39**, 105–180 (2000).
20. Prakash, A. et al. Hybrid molecular beam epitaxy for the growth of stoichiometric $BaSnO_3$. *J. Vac. Sci. Technol. A* **33**, 060608 (2015).
21. Schlom, D. G. Perspective: oxide molecular-beam epitaxy rocks!. *APL Mater.* **3**, 062403 (2015).
22. Smith, E. H. et al. Exploiting kinetics and thermodynamics to grow phase-pure complex oxides by molecular-beam epitaxy under continuous codeposition. *Phys. Rev. Mater.* **1**, 023403 (2017).
23. Song, J. H., Susaki, T. & Hwang, H. Y. Enhanced thermodynamic stability of epitaxial oxide thin films. *Adv. Mater.* **20**, 2528–252 (2008).
24. Petrie, J. R. et al. Strain control of oxygen vacancies in epitaxial strontium cobaltite films. *Adv. Funct. Mater.* **26**, 1564–1570 (2016).
25. Yun, H., Prakash, A., Birol, T., Jalan, B. & Mkhoyan, K. A. Dopant segregation inside and outside dislocation cores in perovskite $BaSnO_3$ and reconstruction of the local atomic and electronic structures. *Nano Lett.* **21**, 4357–4364 (2021).
26. Gorbenko, O. Y., Samoilenkov, S. V., Graboy, I. E. & Kaul, A. R. Epitaxial stabilization of oxides in thin films. *Chem. Mater.* **14**, 4026–4043 (2002).
27. Truttmann, T. K., Liu, F. D., Garcia-Barriocanal, J., James, R. D. & Jalan, B. Strain relaxation via phase transformation in high-mobility $SrSnO_3$ films. *ACS Appl. Electron. Mater.* **3**, 1127–1132 (2021).
28. Bose, A. et al. Effects of anisotropic strain on spin-orbit torque produced by the Dirac nodal line semimetal IrO_2. *ACS Appl. Mater. Interfaces* **12**, 55411–55416 (2020).
29. Liu, J. et al. Strain-induced nonsymmorphic symmetry breaking and removal of Dirac semimetallic nodal line in an orthoperovskite iridate. *Phys. Rev. B* **93**, 085118 (2016).
30. Hou, X., Takahashi, R., Yamamoto, T. & Lippmaa, M. Microstructure analysis of IrO_2 thin films. *J. Cryst. Growth* **462**, 24–28 (2017).
31. Stoerzinger, K. A., Qiao, L., Biegalski, M. D. & Shao-Horn, Y. Orientation-dependent oxygen evolution activities of rutile IrO_2 and RuO_2. *J. Phys. Chem. Lett.* **5**, 1636–1641 (2014).
32. Abb, M. J. S., Herd, B. & Over, H. Template-assisted growth of ultrathin single-crystalline IrO_2(110) films on RuO_2(110)/Ru(0001) and its thermal stability. *J. Phys. Chem. C* **122**, 14725–14732 (2018).

33. Wang, F. & Senthil, T. Twisted Hubbard model for Sr_2IrO_4: magnetism and possible high temperature superconductivity. *Phys. Rev. Lett.* **106**, 136402 (2011).
34. Pesin, D. & Balents, L. Mott physics and band topology in materials with strong spin-orbit interaction. *Nat. Phys.* **6**, 376–381 (2010).
35. Wan, X. G., Turner, A. M., Vishwanath, A. & Savrasov, S. Y. Topological semimetal and Fermi-arc surface states in the electronic structure of pyrochlore iridates. *Phys. Rev. B* **83**, 205101 (2011).
36. Go, A., Witczak-Krempa, W., Jeon, G. S., Park, K. & Kim, Y. B. Correlation effects on 3D topological phases: from bulk to boundary. *Phys. Rev. Lett.* **109**, 066401 (2012).
37. Guo, L. et al. Searching for a route to synthesize in situ epitaxial $Pr_2Ir_2O_7$ thin films with thermodynamic methods. *npj Comput. Mater.* **7**, 144 (2021).
38. Gutierrez-Llorente, A., Iglesias, L., Rodriguez-Gonzalez, B. & Rivadulla, F. Epitaxial stabilization of pulsed laser deposited $Sr_{n+1}Ir_nO_{3n+1}$ thin films: entangled effect of growth dynamics and strain. *APL Mater* **6**, 091101 (2018).

Methods

IrO_2 thin-film growth

Rutile IrO_2 crystallizes in a tetragonal unit cell with lattice parameters $a = b = 4.498$ Å and $c = 3.154$ Å[39]. It has a $P4_2/mnm$ space group (number 136) with non-symmorphic symmetry features (glide and screw symmetries) that give rise to quantum phenomena like the spin Hall effect[40] and topologically non-trivial Dirac nodal lines in the IrO_2 band structure[16]. High-quality epitaxial IrO_2 films have been synthesized using electron beam (e-beam)-assisted MBE[41–43], which can supply Ir vapours by heating the elemental source in excess of 2,000 °C. However, flux control can be challenging with high source temperatures and localized heating provided by the e-beam. With solid-source metal-organic MBE, we circumvent this challenge by replacing pure elemental Ir with a metal-organic precursor $Ir(acac)_3$ that has orders of magnitude higher vapour pressure[44]. This allows Ir supply at source temperatures of less than 200 °C. The metal-organic precursor also helps with metal oxidation as it contains Ir in a pre-oxidized 3+ state. This further eliminates the strict demand on the use of highly reactive ozone as an oxidant.

The IrO_2 thin films were grown using an oxide MBE system (Scienta Omicron) on TiO_2 (110) (Crystec), TiO_2 (101), TiO_2 (001), TiO_2 (100) and α-Al_2O_3 (0001) (*c*-sapphire) substrates (MTI). The substrates were cleaned sequentially in acetone, methanol and isopropanol before being subjected to a baking process at 200 °C for 2 h in a load lock chamber. All substrates were annealed in oxygen plasma for 20 min at growth temperature before film growth. Ir was supplied by sublimation of 99.9% pure $Ir(acac)_3$ (American Elements), an air-stable solid metal-organic powder, which was placed in a crucible (E-Science) inside a custom-built low-temperature effusion cell (E-Science). An effusion cell temperature of 175 °C was used for Ir supply for all samples. For RuO_2 growth, $Ru(acac)_3$ was used as the metal source which was thermally evaporated using a low-temperature effusion cell (MBE Komponenten) at an effusion cell temperature of 180 °C. A radio frequency plasma source (Mantis) with charge deflection plates, operated at a forward power of 250 W, was used for supplying reactive oxygen species required for Ir oxidation. An oxygen pressure ~5×10^{-6} Torr, supplied using a mass flow controller (MKS Instruments), was used for all film growths unless stated otherwise. All films were cooled to 120 °C after growth in the presence of oxygen plasma, to avoid formation of oxygen vacancies and surface decomposition of IrO_2 to Ir metal, as has been reported in literature[32]. We note that owing to a large mean free path of growing species, all reactions during MBE growth occur on the substrate surface.

Characterizing structure and chemical composition

Film surface was monitored during and after growth using reflection high-energy electron diffraction (Staib Instruments). Post growth, films were characterized using XRD and X-ray reflectivity (XRR) (Rigaku Smartlab XE) using Cu K_α radiation ($\lambda = 1.5406$ Å). Film thicknesses were identified using XRR and alternately using thickness fringes (Laue oscillations), if present in the XRD pattern. For film thicknesses lower than 2.5 nm, growth rate was used to estimate the thickness, as no clear XRR pattern could be obtained due to low sample volume. Film surfaces were characterized using AFM (Bruker), optical microscopy (Zeiss) and a field emission gun SEM (JEOL 6500, JEOL USA). SEM-EDX and SEM-EBSD using the JEOL 6500 were used to map the spatial variation of chemical and crystalline composition of the films using an accelerating voltage of 20 kV and 5 kV, respectively. A specimen tilt angle of 70° was used to perform EBSD. The chemical composition of the films was also studied using a laboratory XPS (Physical Electronics, VersaProbe III) setup at a fixed photon energy of 1,486.6 eV.

Synchrotron XRD

Synchrotron XRD measurements including XRR, CTR and in-plane rotational phi scan were carried out on a five-circle Huber diffractometer with Chi geometry using an X-ray energy of 20 keV (wavelength $\lambda = 0.6199$ Å) at the beamline sector 12-ID-D in the Advanced Photon Source at the Argonne National Laboratory. A Si (111) double-crystal monochromator with a resolution $DE/E = 1 \times 10^{-4}$ was used to manipulate and set X-ray energy. The X-ray beam had a total flux of 3×10^{12} photons per second at 20 KeV, and the beam was vertically focused by 1D focusing compound refractive lenses. An X-ray beam profile of 50 µm (*V*) × 500 µm (*H*) was used in the measurement. The scattering signals were captured by a Pilatus 100K 2D area detector, and the 2D images were used to perform the XRR and CTR data processing. Geometric corrections were applied for all XRR and CTR data. XRR data fitting was conducted by the MOTOFit software.

LEEM, LEED and XPS characterization of IrO_2 films with surface Ir features

Thicker IrO_2 films with surface Ir features were further characterized using LEEM, LEED and high-resolution XPS. The LEED, LEEM-IV (I, intensity; V, voltage) and XPS measurements were carried out in the LEEM/X-ray Photoemission Electron Microscopy (XPEEM) endstation of the Electron Spectro-Microscopy (ESM, 21-D-2) beamline at the National Synchrotron Light Source II at Brookhaven National Laboratory. The system has an e-beam spot size of 2 µm in diameter in the LEED mode and a spatial resolution <10 nm in the LEEM mode. The sample was degassed at 120 °C with a pressure of 6×10^{-10} Torr for 1 h. The sample was then annealed at a pressure of 5×10^{-6} Torr of O_2 at 230 °C for 45 min and cooled down in the same pressure of O_2 to room temperature. The surface contaminations on the sample were removed in this procedure, and sharp diffraction patterns were obtained. Our LEEM images show the surface topography of the spot-like features on top of a uniform film background, and their work function difference was calibrated using LEEM-IV with an electron energy in the range of 0–7 eV. The micro-probe LEED-IV data were then acquired from the spot-like features and the film background in the 15–100 eV electron energy range. XPS spectra in the vicinity of Ir 4f states were acquired at a photon energy of 250 eV. The XPS data were analysed in CASA XPS, and the $4f_{5/2}$ and $4f_{7/2}$ peaks for both IrO_2 and Ir were assigned using the literature values found in ref. 45.

SEM, HAADF-STEM and EDX characterization of IrO_2 films

The cross-sectional lamellas for TEM and STEM study were prepared using focused ion beam (FEI Helios NanoLab G4 dual-beam). An am-C layer (~50 nm) was deposited on top of the sample using a sputter coater. Before ion beam trenching, an additional protection layer composed of am-C (2 µm) and Pt (2 µm) was deposited on the region of interest. Focused ion beam was operated at 30 kV with 2 kV e-beam. SEM image was acquired with e-beam at 2 kV and 25 pA. STEM experiments were performed on an aberration-corrected FEI Titan G2 60–300 (S) TEM microscope equipped with a CEOS DCOR probe corrector, monochromator, and a super-X EDX spectrometer. HAADF-STEM images were acquired at 200 kV with 90 pA probe current. Camera length was set to be 130 mm with probe convergence angle of 25.5 mrad for HAADF-STEM imaging. The detector inner and outer collection angles were 55 and 200 mrad, respectively. EDX elemental maps were obtained and quantified via Bruker Esprit.

Electrical transport

Electrical transport measurements were performed in a Van der Pauw geometry using aluminium-wire-bonded contacts in a Quantum Design physical property measurement system. Temperature-dependent resistance measurements were performed from 300 K to 1.8 K. Room temperature resistivities as low as 60 µΩ cm were observed for thicker IrO_2 films, close to the some of the lowest reported values for bulk single crystals (~30 µΩ cm)[39]. Magnetoresistance measurements were performed in a magnetic field range of ±9 T.

Oxygen annealing

Ex situ annealing of the samples was performed in a programmable tube furnace in an oxygen-rich environment. The films were characterized

before and after annealing at each step using XRD and optical microscopy to monitor change in film composition and surface morphology.

DFT calculations

The DFT[46,47] calculations were performed using the generalized gradient approximation for the exchange and correlation and projector augmented potential to describe the interaction between the valence electrons and the ionic cores, as implemented in the VASP code[48–50]. Plane-wave basis was set with a cutoff of 600 eV and k-point meshes equivalent to Γ-centred 8 × 8 × 6 for the 6-atom primitive cell of rutile TiO_2 and IrO_2. The difference in the calculated equilibrium lattice parameters and the experimental values was considered by constraining the in-plane strain to accommodate the experimental values for the in-plane lattice mismatches for the different orientations between the substrates TiO_2 and Al_2O_3 and the epitaxial IrO_2 and Ir bulk. Out-of-plane lattice parameters and all atomic positions were allowed to relax minimizing forces down to 0.001 eV $Å^{-1}$ and total-energy convergence tolerance of 1×10^{-6} eV.

Data availability

The source data for the results of this work can be accessed using the given link: https://doi.org/10.13020/9wm7-x981. Any additional data related to this paper may be requested from the corresponding authors.

References

39. Butler, S. R. & Gillson, J. L. Crystal growth, electrical resistivity and lattice parameters of Ruo_2 and Iro_2. *Mater. Res. Bull.* **6**, 81–88 (1971).
40. Sun, Y., Zhang, Y., Liu, C. X., Felser, C. & Yan, B. H. Dirac nodal lines and induced spin Hall effect in metallic rutile oxides. *Phys. Rev. B* **95**, 235104 (2017).
41. Kawasaki, J. K. et al. Engineering carrier effective masses in ultrathin quantum wells of IrO_2. *Phys. Rev. Lett.* **121**, 176802 (2018).
42. Kawasaki, J. K. et al. Rutile IrO_2/TiO_2 superlattices: a hyperconnected analog to the Ruddlesden–Popper structure. *Phys. Rev. Mater.* **2**, 054206 (2018).
43. Kawasaki, J. K., Uchida, M., Paik, H., Schlom, D. G. & Shen, K. M. Evolution of electronic correlations across the rutile, perovskite, and Ruddlesden-Popper iridates with octahedral connectivity. *Phys. Rev. B* **94**, 121104 (2016).
44. Morozova, N. B., Semyannikov, P. P., Sysoev, S. V., Grankin, V. M. & Igumenov, I. K. Saturated vapor pressure of iridium(III) acetylacetonate. *J. Therm. Anal. Calorim.* **60**, 489–495 (2000).
45. Freakley, S. J., Ruiz-Esquius, J. & Morgan, D. J. The X-ray photoelectron spectra of Ir, IrO_2 and $IrCl_3$ revisited. *Surf. Interface Anal.* **49**, 794–799 (2017).
46. Hohenberg, P. & Kohn, W. Inhomogeneous electron gas. *Phys. Rev.* **136**, 7 (1964).
47. Kohn, W. & Sham, L. J. Self-consistent equations including exchange and correlation effects. *Phys. Rev.* **140**, A1133–A1138 (1965).
48. Kresse, G. & Hafner, J. Ab initio molecular dynamics for liquid metals. *Phys. Rev. B* **47**, 558–561 (1993).
49. Kresse, G. & Hafner, J. Ab initio molecular-dynamics simulation of the liquid-metal–amorphous-semiconductor transition in germanium. *Phys. Rev. B* **49**, 14251–14269 (1994).
50. Kresse, G. & Furthmüller, J. Efficiency of ab-initio total energy calculations for metals and semiconductors using a plane-wave basis set. *Comput. Mater. Sci.* **6**, 15–50 (1996).

Acknowledgements

We thank N. Seaton for help with SEM, EDX and EBSD. Funding for film growth and characterization (S.N., D.L. and B.J.) was supported by the US Department of Energy through DE-SC0020211. S.N. and D.L. acknowledge support from the Air Force Office of Scientific Research (AFOSR) through grant numbers FA9550-21-1-0025 and FA9550-21-0460. S.G., Z.Y. and K.A.M. were supported partially by the UMN MRSEC program under award number DMR-2011401. S.G. and K.A.M. were also supported by SMART, one of seven centres of nCORE, a Semiconductor Research Corporation program, sponsored by the National Institute of Standards and Technology (NIST). Parts of this work were carried out at the Characterization Facility, University of Minnesota, which receives partial support from the National Science Foundation (NSF) through the MRSEC program under award number DMR-2011401. S.J. acknowledges support from the NSF under award number DMR-2129879. W.J. acknowledges support from the US Department of Energy (DOE) Office of Science under DE-SC0023478. R.B.C. acknowledges support from the AFOSR Young Investigator Program under FA9550-20-1-0034. A.J. and A.S. acknowledge support from the NSF through the UD-CHARM University of Delaware Materials Research Science and Engineering Center (number DMR-2011824). The first-principles calculations used Bridges-2 at PSC through allocation DMR150099 from the Advanced Cyberinfrastructure Coordination Ecosystem: Services & Support (ACCESS) program, which is supported by NSF grant numbers 2138259, 2138286, 2138307, 2137603 and 2138296, and the DARWIN computing system at the University of Delaware, which is supported by NSF grant number 1919839. This research used resources of the Center for Functional Nanomaterials and National Synchrotron Light Source II, which are US DOE Office of Science Facilities, at Brookhaven National Laboratory under contract number DE-SC0012704. This research used resources of the Advanced Photon Source, a DOE Office of Science user facility operated for the DOE Office of Science by Argonne National Laboratory under contract number DE-AC02-06CH11357.

Author contributions

S.N. and B.J. conceived the idea and established proof of concept. S.N. grew films and characterized them using XRD, AFM, optical microscopy, SEM and electrical transport measurements. S.N. and B.J. analysed the data. Z.Y. performed magneto-transport measurements and data analysis. D.L. performed XPS measurements. S.G. performed STEM analysis under the supervision of K.A.M. LEEM, LEED and XPS were performed by J.T.S. and analysed by S.J., W.J. and R.B.C. Y.L. and H.Z. carried out synchrotron X-ray diffraction measurements and data analysis. DFT calculations were performed by A.S. under the supervision of A.J. S.N. and B.J. wrote the manuscript. All authors contributed to the discussion and preparation of the manuscript. B.J. directed and organized the different aspects of the project.

Competing interests

The authors declare no competing interests.

Additional information

Supplementary information The online version contains supplementary material available at https://doi.org/10.1038/s41565-023-01397-0.

Correspondence and requests for materials should be addressed to Sreejith Nair or Bharat Jalan.

Peer review information *Nature Nanotechnology* thanks Scott Chambers, Guangwen Zhou and the other, anonymous, reviewer(s) for their contribution to the peer review of this work.